

Singlet fission dynamics modulated by molecular configuration in covalently linked pyrene dimers, *Anti*- and *Syn*-1,2-di(pyrenyl)benzene

Jungkweon Choi^{1,2}, Siin Kim^{1,2}, Mina Ahn³, Jungmin Kim^{1,2}, Dae Won Cho^{1,2}, Doyeong Kim^{1,2}, Seunghwan Eom^{1,2}, Donghwan Im^{1,2}, Yujeong Kim⁴, Sun Hee Kim⁴, Kyung-Ryang Wee³ & Hyotcherl Ihee^{1,2}

Covalently linked dimers (CLDs) and their structural isomers have attracted much attention as potential materials for improving power conversion efficiencies through singlet fission (SF). Here, we designed and synthesized two covalently *ortho*-linked pyrene (Py) dimers, *anti*- and *syn*-1,2-di(pyrenyl)benzene (*Anti*-DPyB and *Syn*-DPyB, respectively), and investigated the effect of molecular configuration on SF dynamics using steady-state and time-resolved spectroscopies. Both *Anti*-DPyB and *Syn*-DPyB, which have different Py-stacking configurations, form excimers, which then relax to the correlated triplet pair ((T₁T₁)) state, indicating the occurrence of SF. Unlike previous studies where the excimer formation inhibited an SF process, the (T₁T₁)'s of *Anti*-DPyB and *Syn*-DPyB are formed through the excimer state. The dissociation of (T₁T₁)'s to 2T₁ in *Anti*-DPyB is more favorable than in *Syn*-DPyB. Our results showcase that the molecular configuration of a CLD plays an important role in SF dynamics.

¹Center for Advanced Reaction Dynamics, Institute for Basic Science, Daejeon 34141, Republic of Korea. ²Department of Chemistry and KI for the BioCentury, Korea Advanced Institute of Science and Technology (KAIST), Daejeon 34141, Republic of Korea. ³Department of Chemistry and Institute of Natural Science, Daegu University, Gyeongsan 38453, Republic of Korea. ⁴Western Seoul Center, Korea Basic Science Institute (KBSI), Seoul 03759, Republic of Korea. ✉email: krwee@daegu.ac.kr; hyotcherl.ihee@kaist.ac.kr

The electron (or charge) carrier dynamics in photoelectric and electrochemical devices are key to determining the performance of devices^{1–6}. Chromophore–chromophore interaction as well as the electronic-state coupling of a chromophore can modulate such electron carrier dynamics^{7–16}. In this regard, many multi-chromophore systems have been widely used for developing highly efficient photoelectric or electrochemical devices using chromophore–chromophore interaction^{7,12–21}. Among the multi-chromophore systems, covalently linked dimers (CLDs) have attracted much attention as potential materials to provide high energy-conversion efficiencies in photovoltaic devices because their excited-state relaxation dynamics, such as the excimer formation, intramolecular charge transfer (ICT), and singlet fission (SF), can be modulated by strategic molecular design^{9,15,22–27}. Especially the dynamics of SF, which is a conversion process from one singlet exciton into two triplet excitons, have been actively investigated with various time-resolved spectroscopies to overcome the limit of Shockley–Queisser power conversion efficiency^{17,28–32}.

The results of extensive studies on SF dynamics and mechanisms showed that they cannot be easily explained by a single unifying mechanism of SF; instead, the intermolecular and intramolecular SF dynamics occur through various types of species such as charge transfer species, excimers, and higher excited vibrational and electronic states, depending on the interactions between chromophores^{21,24–26,29,31,33–37}. For example, Zirzmeier et al. suggested that the SF process occurring in *ortho*-, *meta*-, and *para*-linked pentacene dimers proceed through virtual CT states²⁹. Margulies et al. reported that the covalently linked terylene-3,4:11,12-bis(dicarboximide) (TDI) dimer with a stacked structure forms an excimer within <200 fs, whereas the slip-stacked TDI dimer in a nonpolar solvent forms the correlated triplet pair ((T₁T₁)), which is an intermediate in the SF process³⁰. They also showed that the slip-stacked TDI dimer forms a CT state

in a few picoseconds in a polar solvent, suggesting that adjusting the CT state energy relative to exciton states via solute–solvent interaction can either promote or inhibit SF³⁰. Ni et al. reported that, upon excitation at 250 nm, the cofacial perylene dimer undergoes SF from the upper excited vibrational and electronic states, whereas upon excitation at 450 nm, it fast forms an excimer, which relaxes to the ground state within nanoseconds³⁸. Korovina et al. showed that the *ortho*- and *para*-bis(ethynyltetracenyl)benzene dimers with a relatively stronger through-bond coupling exhibit more efficient SF dynamics than the *meta*-bis(ethynyltetracenyl)-benzene dimer³⁹. Especially, unlike the *ortho*-bis(ethynyltetracenyl)benzene dimer, which forms only (T₁T₁), the *para*-bis(ethynyltetracenyl)benzene dimer shows complete SF dynamics to form free triplets, suggesting that the rotational flexibility between the acenes in the dimers plays an important role in SF dynamics³⁹. Shizu et al. demonstrated that the efficient SF dynamics of *para*-bis(ethynyltetracenyl)benzene dimer is due to large vibronic coupling and the small energy difference between the singlet excited state and the (T₁T₁) state⁴⁰. In contrast, Nakamura et al. showed that in a series of *ortho*-, *meta*-, and *para*-bis(tri isopropyl silylethynyl)-tetracenyl benzene dimers, the *meta*-linked tetracene dimer exhibits more efficient SF dynamics than *ortho*- and *para*-linked tetracene dimers¹⁵. They suggested that the large conformational flexibility and weak electronic coupling play a critical role in their SF dynamics¹⁵. In addition, the experimental and theoretical calculation results of various CLDs showed that compared to *ortho*- and *para*-linked dimers, *meta*-linked dimers exhibit more efficient SF dynamics due to the small binding energy (E_b) of (T₁T₁) ($E_b = 2 E | S_0T_1 \rangle - E | (T_1T_1) \rangle$)^{29,41–43}.

Despite numerous experimental and theoretical approaches to determining the SF dynamics of CLDs, a full understanding of the parameters influencing the SF dynamics of CLDs is still lacking. Additionally, studies on the effects of a molecular configuration, which can affect its excited-state relaxation dynamics, may provide clues for the optimized spatial arrangements that ensure the high-energy conversion efficiency of a real device. In this regard, the role of conformational flexibility in the SF dynamics of CLDs has been studied, but still needs further clarification. Accordingly, in-depth studies are needed to understand their excited-state relaxation dynamics, including SF. From this perspective, we designed and synthesized two covalently *ortho*-linked pyrene (Py) dimers, *anti*- and *syn*-1,2-di(pyrenyl)benzene (*Anti*-DPyB and *Syn*-DPyB) (see Supplementary Methods and Fig. 1 and Supplementary Figs. S1–S6), which we expected to have different configurations, to elucidate the effect of the molecular configuration for their excited-state relaxation dynamics using steady-state and time-resolved spectroscopies. The data show that both *Anti*-DPyB and *Syn*-DPyB form excimers, which rapidly relax to the (T₁T₁) state regardless of solvent polarity, indicating the occurrence of SF dynamics. Notably, the (T₁T₁)s of *Anti*-DPyB in both *n*-hexane and acetonitrile dissociate to free triplets as the end product, completing SF, whereas the dissociation of (T₁T₁)'s in *Syn*-DPyB is less favorable compared with that in *Anti*-DPyB, indicating that the (T₁T₁) of *Syn*-DPyB is more bound with respect to the separated triplets than that of *Anti*-DPyB. Our findings show that the SF dynamics of *Anti*- and *Syn*-DPyB differ due to the different molecular configurations of *Anti*-DPyB and *Syn*-DPyB.

Results

Molecular structures. To characterize the structures of *Anti*-DPyB and *Syn*-DPyB, we calculated their minimum energy structures using density functional theory (DFT). The optimized structures are shown in Fig. 1A. Two Py moieties in *Anti*-DPyB are far from each other, whereas *Syn*-DPyB shows a partial overlap of two pre-stacked Py moieties. According to the calculations using

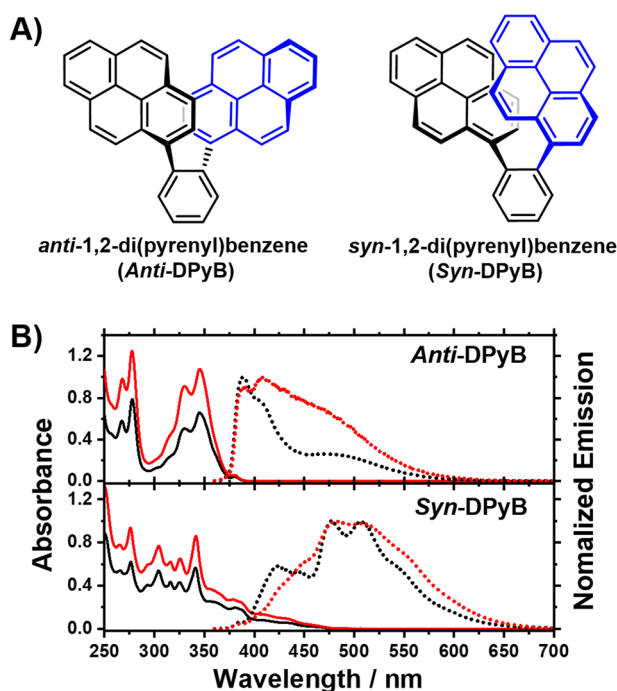


Fig. 1 Structures and UV-visible absorption (solid line) and emission spectra (dotted line). **A** Geometric isomers of *anti*-1,2-di(pyrenyl)benzene (*Anti*-DPyB) and *syn*-1,2-di(pyrenyl)benzene (*Syn*-DPyB). **B** UV-visible absorption spectra of *Anti*-DPyB and *Syn*-DPyB in *n*-hexane (black) and acetonitrile (red). Emission spectra of *Anti*-DPyB and *Syn*-DPyB in *n*-hexane (black) and acetonitrile (red) ($\lambda_{ex} = 345$ nm).

B3LYP/6-31G(d,p), the distances between two Py moieties in *Anti*-DPyB and *Syn*-DPyB are 10.326 and 8.481 Å, respectively (see Supplementary Data 2). This result is consistent with the calculation results reported by Jo et al.⁴⁴ The optimized structure of *Anti*-DPyB obtained from our calculation is similar to its crystal structure (Supplementary Fig. S7, Supplementary Tables S1–S6, and Supplementary Data 1).

Steady-state absorption and emission spectra. As shown in Fig. 1B, *Anti*-DPyB in *n*-hexane and acetonitrile shows two vibrationally resolved absorption bands at around 250–280 and 300–380 nm. This feature is similar to the absorption spectrum of 1-phenylpyrene (Ph-Py)^{9,45}. In contrast, *Syn*-DPyB exhibits a broad and vibrationally resolved absorption band at 250–475 nm. The vibrationally resolved absorption bands observed from *Anti*-DPyB and *Syn*-DPyB indicate that both compounds have highly rigid structures in the ground state. Furthermore, the absorption bands of *Anti*-DPyB and *Syn*-DPyB do not show noticeable dependence on solvent polarity (Fig. 1B).

To investigate the excited-state behaviors of *Anti*-DPyB and *Syn*-DPyB, we measured their emission spectra in *n*-hexane and acetonitrile with excitation at 345 nm, which corresponds to the major absorption peak. *Anti*-DPyB and *Syn*-DPyB in both solvents show dual emission bands (~380 and ~480 nm for *Anti*-DPyB and ~420 and ~480 nm for *Syn*-DPyB), the detailed features of which are different. We checked the possibility that Py molecules are present as impurities in *Anti*-DPyB and *Syn*-DPyB solutions. It is known that the Py molecule shows a strong fluorescence in solutions. Therefore, if Py molecules are present as impurities in *Anti*-DPyB and *Syn*-DPyB solutions, they may contaminate the fluorescence spectra from the *Anti*-DPyB and *Syn*-DPyB samples. To check this possibility, we measured the fluorescence excitation spectra of *Anti*-DPyB and *Syn*-DPyB in acetonitrile at two emission peak positions (380 and 480 nm). As shown in Supplementary Fig. S8, the fluorescence excitation spectra from *Anti*-DPyB and *Syn*-DPyB are significantly different from the absorption spectrum of the Py molecule. This result indicates that Py molecules do not exist as impurities in *Anti*-DPyB and *Syn*-DPyB solutions. The ~380 nm band of *Anti*-DPyB is structured, whereas the broad band centered at ~480 nm is structureless (Fig. 1B). Unlike *Anti*-DPyB, both of the emission bands of *Syn*-DPyB are structured. Based on numerous previous studies on Py and Py derivatives^{46,47}, the shorter-wavelength (~380 and ~420 nm) emissions from *Anti*-DPyB and *Syn*-DPyB can be assigned to Py monomer moieties, and the longer-wavelength (~480 nm for both) emissions to the excimer formed via the association of excited and unexcited Py's. In addition, the broad structureless bands centered at ~480 nm observed for *Anti*-DPyB are highly similar to the typical excimer bands observed for Py and Py derivatives. In terms of solvent dependence, in *Anti*-DPyB, the relative intensities of the emissions from the monomeric Py moiety and excimer show a significant dependence on solvent polarity, whereas *Syn*-DPyB does not show definite solvent dependency.

To accurately determine the singlet energy (E_{S1}) and triplet energy (E_{T1}) values of Py, Ph-Py, *Anti*-DPyB, and *Syn*-DPyB, we also measured emission spectra of Py, Ph-Py, *Anti*-DPyB, and *Syn*-DPyB in MTHF containing iodomethane at 77 K. As shown in Supplementary Fig. S9, all four compounds show dual emission bands at around 370–550 and 580–800 nm, corresponding to fluorescence and phosphorescence, respectively. The E_{S1} values of Py, Ph-Py, *Anti*-DPyB, and *Syn*-DPyB are determined to be 3.3, 3.3, 3.3, and 3.1 eV, respectively. From the phosphorescence spectra, the E_{T1} values of Py, Ph-Py, *Anti*-DPyB, and *Syn*-DPyB are determined to be 2.10, 2.03, 2.04, and 1.87 eV, respectively.

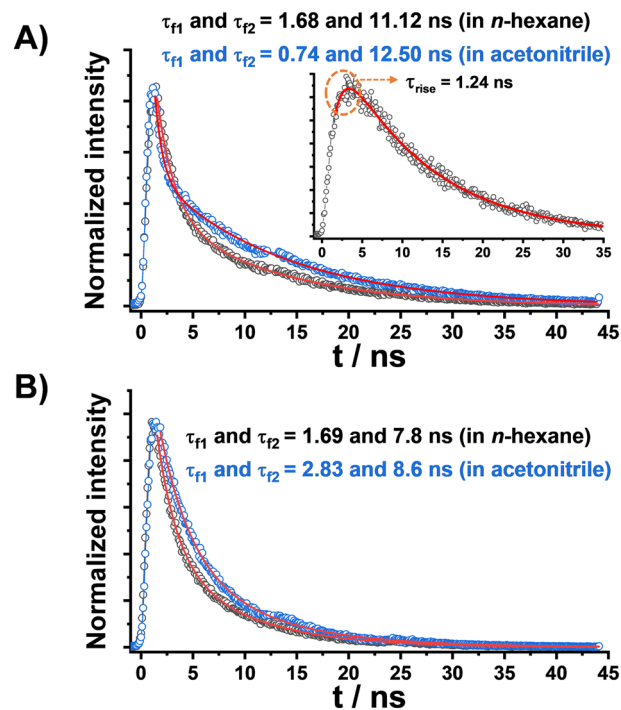


Fig. 2 Fluorescence decay profiles. **A** Fluorescence decay profiles of *Anti*-DPyB in *n*-hexane (black) and acetonitrile (blue), respectively. In **A**, the inset shows the fluorescence decay profile of *Anti*-DPyB measured at the long wavelength (500–600 nm) in *n*-hexane. The fluorescence decay profile of *Anti*-DPyB measured at the long-wavelength (500–600 nm) shows a rise time of 1.24 ns as well as a decay time of 11.1 ns. **B** Fluorescence decay profiles of *Syn*-DPyB in *n*-hexane (black) and acetonitrile (blue), respectively.

Fluorescence lifetime. To further elucidate the excited-state relaxation dynamics, we measured the fluorescence decay profiles of *Anti*-DPyB and *Syn*-DPyB in *n*-hexane and acetonitrile. As depicted in Fig. 2, all decay profiles satisfactorily fit with bi-exponential functions. The determined fluorescence lifetimes are summarized in Table 1. The fast (τ_{f1}) and slow (τ_{f2}) time constants are predominantly observed in the shorter- and longer-wavelength emissions, respectively. Since the shorter- and longer-wavelength emissions arise from the Py monomeric unit and excimer, respectively, the fast (τ_{f1}) and slow (τ_{f2}) time constants correspond to the lifetimes of the Py monomeric unit and excimer, respectively. In addition, as depicted in Fig. 2A, the fluorescence decay profile of *Anti*-DPyB measured in the range of 500–600 nm in *n*-hexane shows an additional kinetic component with a rise time of 1.24 ns.

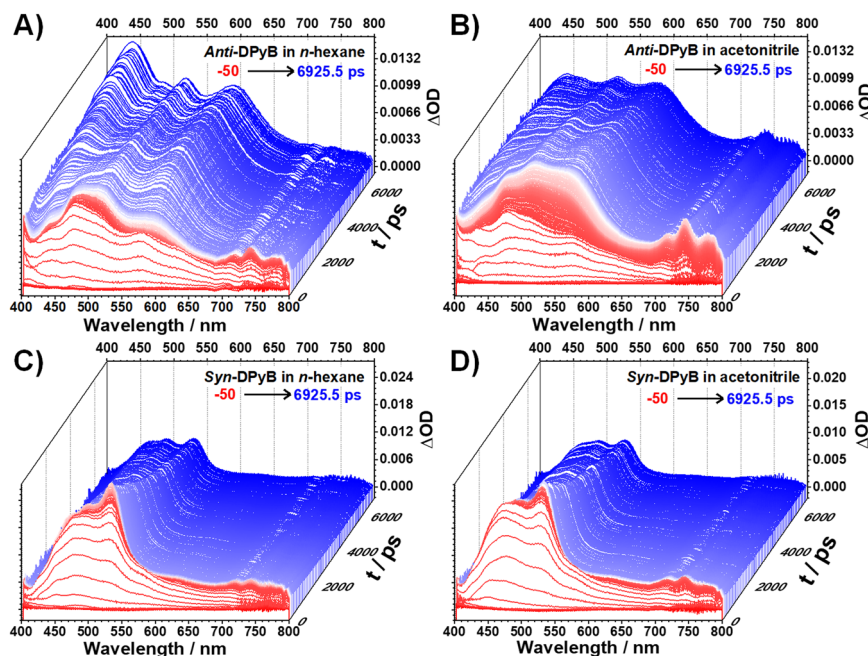
TA spectra. To elucidate the excited-state relaxation dynamics, we measured the femtosecond transient absorption (fs-TA) spectra for *Anti*-DPyB and *Syn*-DPyB in *n*-hexane and acetonitrile with 350 nm excitation. The TA spectra of *Anti*-DPyB in *n*-hexane and acetonitrile exhibit broad signals at 400–700 nm, corresponding to the excited-state absorption (ESA) (see Fig. 3 and Supplementary Fig. S10). With time, these broad positive signals transform into structured signals. On the other hand, the TA spectra of *Syn*-DPyB in *n*-hexane and acetonitrile exhibit intense ESA signals at 450–530 nm with a weak absorption tail (550–700 nm) (Fig. 3C and D). To extract further information, we analyzed the TA spectra of *Anti*-DPyB and *Syn*-DPyB using singular value decomposition (SVD) analysis (Supplementary Information). The SVD analysis for the TA spectra of *Anti*-DPyB and *Syn*-DPyB identified four and three significant singular components, respectively (Supplementary Figs. S11 and S12). As shown in Supplementary Fig. S13, the

Table 1 Emission quantum yields (Φ), emission lifetimes (τ), average emission lifetimes ($\langle\tau\rangle$), radiative rate constants (k_R), and nonradiative rate constants (k_{NR}) of *Anti*-DPyB and *Syn*-DPyB in *n*-hexane and acetonitrile.

		Φ	τ (ns)			k_R^a ($\times 10^7$ s $^{-1}$)	k_{NR}^b ($\times 10^7$ s $^{-1}$)
			τ_{f1}	τ_{f2}	$\langle\tau\rangle$		
<i>Anti</i> -DPyB	In <i>n</i> -hexane	0.20	1.68 \pm 0.03	11.12 \pm 0.11	4.23	4.73	18.9
	In acetonitrile	0.21	0.74 \pm 0.02	12.50 \pm 0.07	3.33	6.31	23.7
<i>Syn</i> -DPyB	In <i>n</i> -hexane	0.09	1.89 \pm 0.04	7.76 \pm 0.10	3.59	2.51	25.3
	In acetonitrile	0.14	2.93 \pm 0.10	8.64 \pm 0.21	4.87	2.87	17.7

$$^a k_R = \Phi / \langle\tau\rangle.$$

$$^b k_{NR} = (1 - \Phi) / \langle\tau\rangle.$$

**Fig. 3** Transient absorption spectra. **A, B** Transient absorption spectra of *Anti*-DPyB in *n*-hexane and acetonitrile, respectively. **C, D** Transient absorption spectra of *Syn*-DPyB in *n*-hexane and acetonitrile, respectively.

significant rSVs for *Anti*-DPyB in *n*-hexane and acetonitrile can be expressed by a tetra-exponential function with shared relaxation times (3.6 \pm 0.3, 231 \pm 19 ps, 1.75 \pm 0.12 ns, and >10 ns in *n*-hexane; 2.8 \pm 0.1, 24.3 \pm 0.5, 495.7 \pm 6.5 ps, and >10 ns in acetonitrile). The significant rSVs for *Syn*-DPyB in *n*-hexane and acetonitrile can be expressed by a tri-exponential function with shared relaxation times (2.3 \pm 0.8, 9.7 \pm 0.5 ps, and 6.4 \pm 0.2 ns in *n*-hexane; 2.8, 8.0 \pm 0.6 ps, and 4.8 \pm 0.2 ns in acetonitrile). The time constants are summarized in Table 2.

To observe the long-lived species, we measured the nanosecond TA spectra of *Anti*-DPyB and *Syn*-DPyB in *n*-hexane and acetonitrile with 355 nm excitation. *Anti*-DPyB in *n*-hexane and acetonitrile shows a weak and broad absorption band around 445 nm at a time delay of a few microseconds (Supplementary Fig. S14), suggesting the presence of a long-lived species. In contrast, *Syn*-DPyB does not exhibit any absorption band in both *n*-hexane, and acetonitrile, indicating that no long-lived species, such as a triplet species, exist at the μ s–ms time scale.

Discussion

Intramolecular excimer formation and electronic coupling.

The optimized structures of *Anti*-DPyB and *Syn*-DPyB show that the distance between two Py moieties in *Anti*-DPyB is longer than

that in *Syn*-DPyB, suggesting that the interaction in *Anti*-DPyB between two Py moieties should be weaker than that in *Syn*-DPyB with the partial overlap of two Py moieties. *Anti*-DPyB has an absorption spectrum similar to that of Py or Ph-Py^{9,45}, indicating that in the ground state, the two Py moieties in *Anti*-DPyB have a monomeric character. In contrast, the pre-stacked structure of *Syn*-DPyB is expected to show the characteristic feature of an excimer. Indeed, *Syn*-DPyB exhibits a single broad and vibrationally resolved absorption band at 250–475 nm owing to the strong π - π interaction between the two Py moieties. The steady-state spectroscopic results confirm this prediction: in the ground state, the interaction between the two Py moieties in *Anti*-DPyB is much weaker than that in *Syn*-DPyB. On the other hand, the cyclic voltammograms for the reduction of *Anti*-DPyB and *Syn*-DPyB in THF show two separate peaks, whereas the cyclic voltammogram of Py exhibits a single peak (Supplementary Fig. S15). From the cyclic voltammograms, the splitting energies ($E_{red2} - E_{red1}$) of *Anti*-DPyB and *Syn*-DPyB are determined to be 0.09 and 0.12 V, respectively (Table 3). Compared to *Syn*-DPyB, the lower splitting energy of *Anti*-DPyB indicates that the electronic coupling between the two Py moieties in *Anti*-DPyB is relatively weaker than that in *Syn*-DPyB. This result is consistent with the steady-state spectroscopic results.

Table 2 Time constants determined from TA measurements for Anti-DPyB and Syn-DPyB in *n*-hexane and acetonitrile^a.

		τ_1 (ps)	τ_2 (ps)	τ_3 (ps)	τ_4^a (ns)	τ_5^a (ns)
<i>Anti</i> -DPyB	In <i>n</i> -hexane	3.6 ± 0.3	231 ± 19	1750 ± 116	>10	>10
	In acetonitrile	2.8 ± 0.1	24.3 ± 0.5	495.7 ± 6.5	>10	>10
<i>Syn</i> -DPyB	In <i>n</i> -hexane	2.3 ± 0.8	-	9.7 ± 0.5	6.4 ± 0.2	-
	In acetonitrile	2.8	-	8.0 ± 0.6	4.8 ± 0.2	-

^aThe (T_1T_1) has two fates: the decay to the ground state (τ_4) and the dissociation to free triplets (τ_5). We could not distinguish two process because the lifetime of (T_1T_1) is longer than the investigated delay times. Thus we denote two time constants for the decay to the ground state and the dissociation to free triplets as >10 ns.

Table 3 Electrochemical parameters of Py, Anti-DPyB and Syn-DPyB evaluated by cyclic voltammograms (E_{ox1} and E_{ox2} : first and second oxidation potentials, E_{red1} and E_{red2} : first and second reduction potentials).

	$E_{ox1}^{a,b}$ (V)	$E_{ox2}^{a,b}$ (V)	$E_{red1}^{a,c}$ (V)	$E_{red2}^{a,c}$ (V)	$E_{ox2} - E_{ox1}$ (V)	$E_{red2} - E_{red1}$ (V)
Py	0.85		-2.22			
<i>Anti</i> -DPyB	0.83	0.98	-2.07	-2.16	0.15	0.09
<i>Syn</i> -DPyB	0.85	1.12	-2.06	-2.18	0.27	0.12

^aDetermined by cyclic voltammetry (vs. SCE).

^bMeasured in CH_2Cl_2 .

^cMeasured in THF

We note that the excimer formation in *Anti*-DPyB and *Syn*-DPyB is intramolecular. The emission spectra of *Anti*-DPyB and *Syn*-DPyB are not influenced by the solute concentration (Supplementary Fig. S16). This result confirms that the excimers in *Anti*-DPyB and *Syn*-DPyB form due to intramolecular rather than intermolecular interaction. Because, in *Anti*-DPyB, the interaction between the two Py moieties in the ground state is weak due to the long distance between the two chromophores with twisted alignment, the intramolecular excimer formation requires the rearrangement of two distant Py moieties. This scenario is consistent with the flexible structure of the excimer of *Anti*-DPyB, reflected in its broad structureless excimer emission band (~480 nm). In contrast, *Syn*-DPyB is expected to rapidly form an excimer with no or less structural rearrangement because of the partial overlap of the two Py moieties. Based on the structured excimer emission band (~480 nm) of *Syn*-DPyB, we suggest that the excimer structure is as rigid as the structure in the ground state.

The solvent dependence on the emission spectra of *Anti*-DPyB can be rationalized by considering the following scenario: As Py is a hydrophobic molecule, two Py moieties in a nonpolar solvent show monomeric behavior, whereas a high polarity solvent facilitates the hydrophobic interaction of two Py moieties, resulting in more efficient excimer formation. The absence of solvent dependence on the emission of *Syn*-DPyB is probably due to its rigid structure owing to the strong π - π interaction between two Py moieties. The solvent dependency on the emission of *Anti*-DPyB and *Syn*-DPyB can be also interpreted in terms of the change in the dipole moment (μ) induced by the structural change in the excited state. The solvent dependency on the emission of *Anti*-DPyB suggests that the $\Delta\mu$ ($=\mu_e - \mu_g$) value for *Anti*-DPyB is likely larger than that for *Syn*-DPyB. The DFT calculation, which was performed using CAM-B3LYP-D3/6-31G**³⁸, shows that the dipole moments (μ_g) of *Anti*-DPyB and *Syn*-DPyB in the ground state are 0.021 and 0.1394 D, respectively (see Supplementary Data 2). According to the TDDFT calculation, the dipole moments (μ_e) of the optimized *Anti*-DPyB and *Syn*-DPyB in the excited state are 0.3052 and 0.2729 D, respectively. These TDDFT/DFT calculations demonstrate that the $\Delta\mu$ (0.284 D) of *Anti*-DPyB is larger than that of *Syn*-DPyB (0.134 D), suggesting that in the excited state, the structural change in *Anti*-DPyB to form the excimer may induce a relatively large $\Delta\mu$ compared to that of *Syn*-DPyB. Unlike *Anti*-DPyB and

Syn-DPyB that form the excimer in the excited state, 1,4-di(1-pyrenyl)benzene (Py-Benz-Py), which is a covalently *para*-linked pyrene (Py) dimer, shows significant different excited-state relaxation dynamics⁹. Indeed, it was reported that Py-Benz-Py exhibits solvent-dependent ICT dynamics, followed by the twisting motion between Py and phenyl moieties, without intramolecular excimer formation⁹. The difference in the excited-state relaxation dynamics of *Anti*-DPyB, *Syn*-DPyB, and Py-Benz-Py indicates that the molecular structure and configuration play a vital role in their excited-state relaxation dynamics.

Excited-state dynamics dependent on molecular configuration.

As shown in Table 2, the TA data for both *Anti*-DPyB and *Syn*-DPyB show similar τ_1 time constants (2.3–3.7 ps) regardless of solvent polarity. This time scale falls into the well-known time scale for vibrational relaxation. Thus, the earliest kinetic component (τ_1) of ~3 ps can be interpreted as the intramolecular vibrational relaxation (IVR) from the initially populated local excited state (Franck-Condon state).

After IVR (τ_1), the excited molecules in the S_1 state have various potential fates, including relaxation to other excited states, such as excimer or triplet excited states, and returning to the ground state via fluorescence. The observation of excimer fluorescence for *Anti*-DPyB and *Syn*-DPyB leads to the interpretation that a part of the excited molecules in the S_1 state relaxes to the excimer state. As discussed above, the excimer formation in *Anti*-DPyB should require the rearrangement of the two distant Py moieties to induce the interaction between them. In this regard, the τ_2 time constants observed from *Anti*-DPyB can be interpreted as conformational change. The τ_2 time constant (231 ps) of *Anti*-DPyB in *n*-hexane is similar to the 323 ps assigned to the twisting motion between the Py and phenyl moiety of Py-Benz-Py⁹ in a nonpolar solvent. Thus, we attribute the τ_2 of *Anti*-DPyB to excimer formation via $S_1 \rightarrow$ excimer transition accompanying the twisting motion between the Py and phenyl moieties. The faster excimer formation in acetonitrile probably occurs due to the strong hydrophobic interaction between the two Py moieties in a high-polarity solvent. The excimer of *Anti*-DPyB decays to a long-lived species with τ_3 time constants. The TA spectra of the long-lived species are highly similar to the triplet-triplet absorption spectra of free Py derivatives corresponding to the $T_1 \rightarrow T_n$ transition^{48,49}.

Specifically, the long-lived species of *Anti*-DPyB show structured TA spectra, similar to the T_1 -to- T_n absorption spectra for carbonylpyrenes reported by Rajagopal et al.⁴⁹ Furthermore, the TA signals of *Anti*-DPyB observed at >5 ns resemble the T_1 -to- T_n absorption spectrum of 1-(2-bromophenyl)pyrene measured in dichloromethane (DCM) (Supplementary Fig. S17), although the peak positions are slightly different from each other. Therefore, the long-lived species observed in *Anti*-DPyB are T_1 (free triplet state) or a similar state that produces an absorption spectrum similar to that of T_1 -to- T_n .

The second fastest time constant (9.7 and 8.0 ps in *n*-hexane and acetonitrile, respectively) for *Syn*-DPyB is faster than that for *Anti*-DPyB by two orders of magnitude. Nevertheless, these time scales are much longer than the typical subpicosecond time scale reported for the excimer formation of prestacked dimeric systems^{24,30}. For example, Hong et al. showed that the excimer state of cofacial stacked perylene bisimide dimer is formed within 200 fs²⁴. Unlike *Anti*-DPyB, the excimer in *Syn*-DPyB with a prestacked structure should be rapidly formed with no or less structural rearrangement. For this reason, we ruled out the possibility that the second fastest time constants in *Syn*-DPyB can be attributed to excimer formation dynamics. Instead, we consider two possibilities: the excited molecules in S_1 formed by IVR (~ 3 ps) relax to the excimer state (i) within a subpicosecond (≤ 200 fs) and (ii) with a time constant comparable to IVR (~ 3 ps). Notably, the TA spectra of a long-lived species formed with the second fastest time constants in *Syn*-DPyB are highly similar to the triplet-triplet absorption spectra of free Py derivatives corresponding to the $T_1 \rightarrow T_n$ transition, like those of a long-lived species formed with τ_3 time constants in *Anti*-DPyB. For this reason, we denote the time constants of 9.7 and 8.0 ps for *Syn*-DPyB as τ_3 , not τ_2 . In other words, the long-lived species in *Anti*-DPyB and *Syn*-DPyB are formed with τ_3 time constants and they are attributed to T_1 or a similar state.

The free triplet states of a molecule can be generated through an ISC process or the dissociation of (T_1T_1). It has been accepted that the ISC process in organic molecules with a small spin-orbit coupling occurs with a timescale of 10 ns to 1 ms and the lifetime of the triplet state is longer than the timescale in the order of 1 μ s. In contrast to ISC, (T_1T_1) rapidly forms within the range of 10 fs to 1 ns and has a significantly shorter lifetime than that of the free triplet formed via the ISC process, although the TA spectrum for the (T_1T_1) is similar to that of the free triplet formed through ISC. A previous study of Py in micelles reported an ISC time constant of 1.7 μ s⁵⁰, which is much longer than the τ_3 time constants of 1.75 ns and 495.7 ps for the formation of the long-lived species of *Anti*-DPyB in *n*-hexane and acetonitrile, respectively. Meanwhile, the long-lived species for *Syn*-DPyB in *n*-hexane and acetonitrile are formed with τ_3 time constants of 9.7 and 8.0 ps, respectively, and then relax to other states with τ_4 time constants of 6.4 and 4.8 ns, respectively. These lifetimes of the long-lived species of *Anti*-DPyB and *Syn*-DPyB are significantly shorter than the triplet lifetimes of Py (9.4–11 ms)⁵¹. Thus, we attribute the long-lived species observed from *Anti*-DPyB and *Syn*-DPyB to the (T_1T_1) formed through the first step of SF. Similar examples were reported for the SF dynamics of bis(triisopropylsilylethynyl)-tetracene (Tips-tetracene) in solution, which occur via an excimer with a (T_1T_1) character³⁴, and four 3,6-bis(thiophene-2-yl)diketopyrrolopyrrole derivatives with different substituents in film, which involve an intermediate excimer-like state⁵². However, it has been generally accepted that excimer formation inhibits an SF process^{30,38}. Contrary to this generally accepted view, our results demonstrate that the excimers in both *Anti*-DPyB and *Syn*-DPyB are rapidly converted to (T_1T_1). $2E_{T_1}$ values of *Anti*-DPyB (4.08 eV) and *Syn*-DPyB (3.74 eV) are higher than their E_{S_1} values (3.3 and 3.1 eV, respectively), suggesting that the SF processes in *Anti*-DPyB and *Syn*-DPyB are endothermic reactions.

Singlet fission. The dissociation dynamics of (T_1T_1) in the SF process is key to determining the energy conversion efficiency in photoelectric or electrochemical devices, as the faster dissociation of (T_1T_1) to free triplets is preferable in terms of energy conversion efficiency. The nanosecond TA experiments for *Anti*-DPyB and *Syn*-DPyB provide a clue for the free triplet that can be generated by the dissociation dynamics of (T_1T_1). The nanosecond TA spectra for *Anti*-DPyB and *Syn*-DPyB suggest that the triplet species of *Anti*-DPyB exists at the μ s–ms time scale, whereas *Syn*-DPyB does not exhibit any absorption band in both *n*-hexane and acetonitrile at this time scale. As shown in Supplementary Figs. S14 and S18, the absorption band around 445 nm of *Anti*-DPyB measured from the nanosecond TA experiment is similar to the T_1 -to- T_n absorption spectrum of 1-(2-bromophenyl)pyrene measured in DCM (Supplementary Fig. S17), suggesting that the chemical species of *Anti*-DPyB observed at the μ s–ms time scale are attributed to T_1 . To further confirm our interpretation, we additionally performed the nanosecond TA experiment for *Anti*-DPyB in iodomethane to maximize the heavy atom effect. As shown in Supplementary Fig. S18A, *Anti*-DPyB in iodomethane exhibits an intense absorption band in the range of 350–600 nm at a 1 μ s time delay, which is almost identical to those of *Anti*-DPyB measured in *n*-hexane and acetonitrile using femtosecond TA spectroscopy. Thus, we suggest that the chemical species of *Anti*-DPyB observed at the μ s–ms time scale are the free triplets generated by the dissociation dynamics of (T_1T_1). Furthermore, we performed the nanosecond TA experiment for Py, Ph-Py, and *Syn*-DPyB in iodomethane. Their TA spectra show absorption bands in the range of 350–600 nm at a 1 μ s time delay (Supplementary Fig. S18B). The absorption band of *Syn*-DPyB measured in *n*-hexane and acetonitrile using femtosecond TA spectroscopy is similar to the T_1 -to- T_n absorption band of *Syn*-DPyB measured in iodomethane. In this regard, the last relaxation times (τ_4) observed from *Anti*-DPyB and *Syn*-DPyB by femtosecond TA experiments are attributed to the dissociation dynamics of (T_1T_1).

On the other hand, the (T_1T_1) has two fates: (i) dissociation to free triplets and (ii) decay to the ground state (Fig. 4). The femtosecond TA measurements showed that the time profile for transient absorption bands of *Anti*-DPyB around 440 nm, which well reflects the relaxation kinetics of (T_1T_1), shows slow but distinct rising features (Supplementary Fig. S19A), whereas *Syn*-DPyB shows a relatively fast relaxation dynamics of (T_1T_1) to $2T_1$ and S_0 in parallel with a few nanosecond time constants (Supplementary

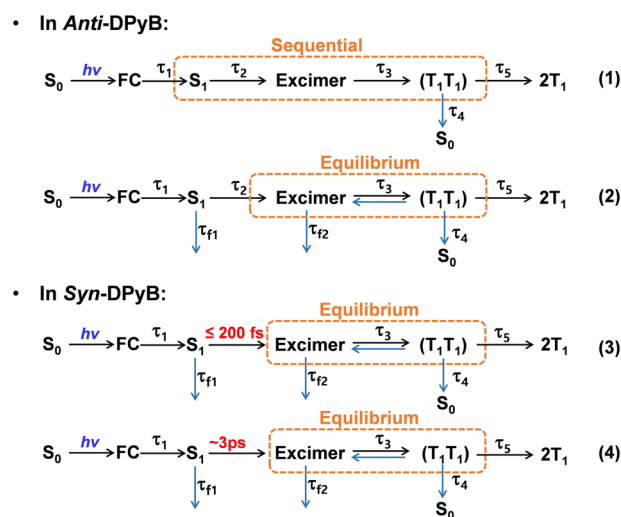


Fig. 4 Kinetic schemes for photoinduced reactions of *Anti*-DPyB and *Syn*-DPyB. S_0 : ground state, FC: Franck–Condon state, S_1 : singlet excited state, (T_1T_1): correlated triplet pair, and T_1 : free triplet state.

Fig. S19B and Table 2). This difference in the time profiles of *Anti*-DPyB and *Syn*-DPyB suggests that the (T_1T_1) of *Anti*-DPyB dissociates dominantly into $2T_1$, whereas the (T_1T_1) of *Syn*-DPyB decays mainly to S_0 state. Using the data from nanosecond TA spectroscopy, the triplet quantum yield (Φ_T) values of *Anti*-DPyB in *n*-hexane and acetonitrile are determined to be 44.1% and 17.5%, respectively (Supplementary Methods). Meanwhile, we could not determine the Φ_T values of *Syn*-DPyB in *n*-hexane and acetonitrile, suggesting that the dissociation reaction of (T_1T_1) in *Syn*-DPyB is significantly suppressed compared to *Anti*-DPyB and the (T_1T_1) of *Syn*-DPyB decays mainly to S_0 state. The suppressed dissociation of (T_1T_1) into free triplets in *Syn*-DPyB is probably due to triplet-triplet annihilation (TTA), which can be facilitated by the proximity of two Py moieties in the excimer state. Several studies of SF suggested that TTA is one of the decay processes of (T_1T_1)^{17,53–55}. The TTA results in two fates: decay to the ground state and upconversion to a higher excited singlet state (excimer). The suppressed dissociation of (T_1T_1) into free triplets in *Syn*-DPyB is probably due to TTA. Since the upconversion to the excimer state proceeds on a time scale in the tens of picoseconds, we attribute the τ_4 of *Syn*-DPyB to the (T_1T_1) \rightarrow S_0 relaxation dynamics.

To confirm the SF dynamics, we performed time-resolved electron paramagnetic resonance (TR-EPR) measurements for *Anti*-DPyB and *Syn*-DPyB. The X-band (9.728 GHz) perpendicular mode TR-EPR spectra of *Anti*-DPyB and *Syn*-DPyB in toluene were measured at 80 K. Supplementary Fig. S20 shows EPR spectra of *Anti*-DPyB and *Syn*-DPyB at 128 and 200 ns after photoirradiation. The EPR signals for *Anti*-DPyB and *Syn*-DPyB show the narrow peak splitting of 34 and 19 mT around 340 mT ($g = 2.002$), respectively. In addition to the narrow peak splitting, *Anti*-DPyB and *Syn*-DPyB exhibit a large peak splitting of 150 and 115 mT, respectively. The EPR signals for *Anti*-DPyB and *Syn*-DPyB are well reproduced by the simulated curve for its triplet (see Supplementary Information). We further confirmed the origins of TR-EPR signals via the nutation experiment for the Q-band (34 GHz) TR-EPR signal of *Anti*-DPyB (see Supplementary Fig. S21). Although the nutation measurement on the EPR signal of *Syn*-DPyB was not performed, we speculate that the X-band EPR signal measured from *Syn*-DPyB arises from triplet species as well. The EPR signals at a few hundred nanoseconds do not show evidence for (T_1T_1). The absence of EPR signals of (T_1T_1) for *Anti*-DPyB and *Syn*-DPyB at a few hundred nanoseconds is probably due to the shorter lifetimes of (T_1T_1)s than the temporal resolution (~ 120 ns) of our TR-EPR system. *Syn*-DPyB shows a relatively fast decay feature in the time profile for TA bands of 450 nm (Supplementary Fig. S19B). As shown in Table 2, the (T_1T_1)s of *Syn*-DPyB in *n*-hexane and acetonitrile relax to $2T_1$ and S_0 in parallel with time constants of 6.4 and 4.8 ns, respectively, indicating that the lifetime of (T_1T_1) for *Syn*-DPyB should be significantly shorter than the temporal resolution (~ 120 ns) of our TR-EPR system. Meanwhile, we could not precisely determine the lifetime of (T_1T_1) for *Anti*-DPyB because of the limited range of investigated delay times in the femtosecond TA measurement. Overall, the EPR data lead us to conclude that the lifetime of (T_1T_1) for *Anti*-DPyB should be shorter than the temporal resolution (~ 120 ns) of our TR-EPR system.

The difference in the SF dynamics of *Anti*-DPyB and *Syn*-DPyB may be interpreted in terms of the E_b of (T_1T_1). According to the kinetic model for SF proposed by Kolomeisly et al., the rates of the formation and dissociation of (T_1T_1) depend on E_b ⁵⁶. They defined that if $E_b > 0$, then the (T_1T_1) state is bound, and if $E_b < 0$, then it is unbound. The (T_1T_1) destabilization ($E_b < 0$) simultaneously results in the fast dissociation of (T_1T_1) and the slow formation of (T_1T_1). Based on a spin-lattice model, Abraham and Mayhall predicted that in various covalently linked tetracene or pentacene dimers⁴², the (T_1T_1) state of the *meta*-

linked dimer would be unbound with respect to the separated triplets due to the smaller or negative E_b compared to those of the *ortho*- and *para*-linked dimers, whereas the (T_1T_1) states of the *ortho*- and *para*-linked dimers would be bound. Similarly, the analysis of wave functions by Chesler et al. showed that the slow formation of (T_1T_1) in *meta*-bianthracene may be due to the small or negative E_b , whereas the fast formation of (T_1T_1) of *para*-bianthracene results from the larger or positive E_b ⁴¹. In other words, these theoretical studies predicted that compared to *ortho*- and *para*-linked dimers, *meta*-linked dimers with a smaller E_b would exhibit a relatively slower formation of (T_1T_1) state and a relatively fast dissociation of (T_1T_1) into free triplets with a large yield. Indeed, the experimental results for several CLDs agree with the theoretical predictions^{29,41–43}. The theoretical calculation results for many *ortho*-linked CLDs predict that *Anti*-DPyB and *Syn*-DPyB, which are also *ortho*-linked CLDs, form the bound (T_1T_1) state due to the large or positive E_b . The TA data demonstrate that *Syn*-DPyB shows a low dissociation reaction of the (T_1T_1) into free triplets, suggesting that the (T_1T_1) state of *Syn*-DPyB is relatively bound compared to that of *Anti*-DPyB. In contrast to *Syn*-DPyB, *Anti*-DPyB shows a significantly slower formation of (T_1T_1) followed by the dissociation into free triplets, suggesting that the (T_1T_1) state of *Anti*-DPyB is unbound. This result indicates that as with *meta*-linked dimers that show favorable SF dynamics, *Anti*-DPyB, even if it is an *ortho*-linked dimer, forms the unbound (T_1T_1) state due to a small or negative E_b , leading to the efficient dissociation of (T_1T_1) into free triplets. The theoretical calculation results by Nakano and coworkers demonstrated that compared to *ortho*- and *para*-linked pentacene dimers, the electronic coupling between chromophores for the *meta*-linked pentacene dimer is very low, resulting in the relatively slow formation of (T_1T_1) and an efficient SF^{57,58}. In this regard, the efficient SF in *Anti*-DPyB is due to the low electronic coupling owing to the twisted alignment of the two chromophores. This result indicates that the SF dynamics in *ortho*-linked dimers, which show a significant π -orbital overlap between two chromophores, can be modulated by controlling the molecular configuration. Consequently, our results for *Anti*-DPyB and *Syn*-DPyB suggest that the molecular geometry of a CLD plays a critical role in their SF dynamics as well as excimer formation and ICT.

TA spectra analysis with kinetic models. We performed the kinetic analysis of the TA spectra of *Anti*-DPyB and *Syn*-DPyB considering various plausible kinetic models. For *Anti*-DPyB, considering five principal components from SVD analysis (Supplementary Fig. S11) and four-time constants obtained from the fitting of rSVs (Supplementary Fig. S13), we set up the simplest kinetic model with five intermediates assigned to FC, S_1 , excimer, (T_1T_1), and $2T_1$, and the four-time constants connecting them. Considering the relaxation process of the (T_1T_1) state into $2T_1$ and S_0 , the decay process from (T_1T_1) to S_0 was added to the kinetic model. The resulting kinetic model is Kinetic Model (1) in Fig. 4. Details regarding Kinetic Model (1) are provided in Supplementary Information.

Whereas Kinetic Model (1) could explain the TA data well, it could not explain the emission behavior. The fluorescence decay profiles showed two-time constants assigned to the fluorescence lifetimes of the Py monomeric unit and excimer. By adding these two fluorescence decay times to Kinetic Model (1), we set up a different kinetic model (Kinetic Model (2) in Fig. 4). In this kinetic model, we also included the backreaction from (T_1T_1) to the excimer for the following reason: As shown in the inset of Fig. 2A, the rising time of 1.24 ns in the fluorescence decay profile for *Anti*-DPyB in *n*-hexane is approximately five times larger than the time

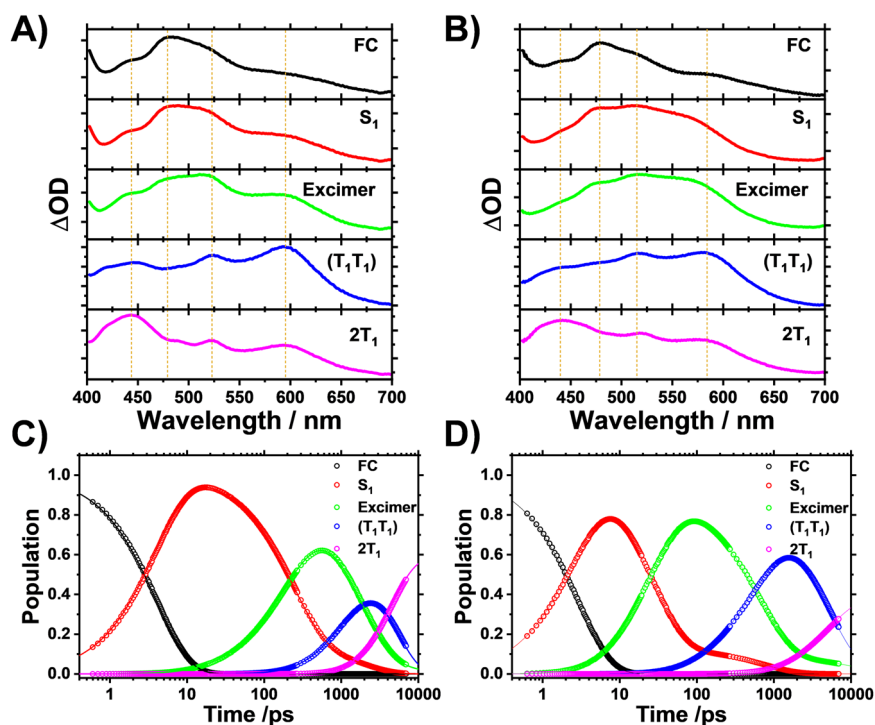


Fig. 5 Species-associated difference spectra and population changes of intermediates for *Anti-DPyB* obtained from the kinetic analysis for Kinetic Model (2) in *n*-hexane and acetonitrile. **A, B** Species-associated difference spectra in **A** *n*-hexane and **B** acetonitrile. **C, D** Population changes of intermediates in **C** *n*-hexane and **D** acetonitrile. The solid lines are the concentrations obtained from the kinetics analysis. The open circles represent the measure time delays.

constant (0.23 ns) corresponding to the $S_1 \rightarrow$ excimer transition determined from femtosecond TA experiments. This difference indicates that the observed excimer fluorescence is not prompt emission but delayed emission, suggesting equilibrium between the excimer state and the (T_1T_1) state. Details regarding Kinetic Model (2) are provided in Supplementary Information. Figure 5 shows the five SADS curves and population changes for five intermediates (FC, S_1 , excimer, (T_1T_1) , and $2T_1$) obtained from the kinetic analysis for Kinetic Model (2), and Supplementary Fig. S24 shows the experimental TA spectra, the best-fit spectra, and the residuals between them for *Anti-DPyB* in *n*-hexane and acetonitrile obtained from the kinetic analysis using Kinetic Model (2). The residuals between the experimental and the best-fit spectra are small, suggesting that the measured TA spectra for *Anti-DPyB* are well constructed as a linear combination of the five SADS curves according to the employed kinetic model. As the fit qualities of both Kinetic Models (1) and (2) are comparable, fit qualities alone could not be used to determine which kinetic model is more accurate (Supplementary Figs. S22–S24). As discussed above, however, Kinetic Model (2) is preferred because it is more consistent with the emission data.

For *Syn-DPyB*, considering the three exponential time constants obtained from the exponentials fitting of rSVs (Supplementary Fig. S13), the two-time constants and emission quantum yields from the emission experiments (Table 1), and the four principal components from SVD analysis results (Supplementary Fig. S12), we can preferentially set up a kinetic model with five-time constants and four intermediates. Simultaneously, the TR-EPR signal for *Syn-DpyB* indicates that the (T_1T_1) of *Syn-DPyB* also dissociates to free triplets. Based on this result, the $(T_1T_1) \rightarrow 2T_1$ transition was included in the kinetic model. We also included the backreaction from (T_1T_1) to the excimer as in *Anti-DPyB*. Consequently, as in *Anti-DPyB*, we used the kinetic model with five intermediates assigned to FC, S_1 , excimer, (T_1T_1) , and $2T_1$

(see Fig. 4). In the case of *Syn-DPyB*, it is noteworthy that the τ_2 time constant corresponding to the $S_1 \rightarrow$ excimer transition was not observed in *Syn-DPyB* (Table 2). The excimer of *Syn-DPyB* with a pre-stacked structure likely forms quickly within a subpicosecond (≤ 200 fs) or with a time constant comparable to the IVR (~ 3 ps). In this regard, we considered two kinetic models (Kinetic Models (3) and (4) in Fig. 4). In the former kinetic model, the $S_1 \rightarrow$ excimer transition occurs in a subpicosecond (≤ 200 fs), and in the other kinetic model, the $S_1 \rightarrow$ excimer transition occurs with a time constant comparable to the IVR (~ 3 ps). As shown in Supplementary Figs. S25 and S26, both Kinetic Models (3) and (4) show small residuals between the experimental and the best-fit spectra, suggesting that the measured TA spectra for *Syn-DPyB* are well constructed as linear combinations of the five SADS curves according to both kinetic models, and that fit qualities alone cannot be used to determine which kinetic model is better. Nevertheless, the SADS curves from the two kinetic models are different and provide clues regarding which kinetic model is more accurate. Whereas the SADS for the S_1 state from Kinetic Model (4) is positive (Fig. 6), that from Kinetic Model (3) is strongly negative (Supplementary Fig. S25), which is not possible for excited state absorption (ESA) from the S_1 state, so Kinetic Model (3) could be ruled out. In other words, the kinetic analysis suggests that the $S_1 \rightarrow$ excimer transition in *Syn-DPyB* occurs with a time constant comparable to the IVR (~ 3 ps). Figure 6 shows the five SADS curves and population changes for five intermediates (FC, S_1 , excimer, (T_1T_1) , and $2T_1$) for *Syn-DPyB* obtained from the kinetic analysis for Kinetic Model (4) in *n*-hexane and acetonitrile. The small differences among SADS curves of *Syn-DPyB* are probably due to the rigid structure of *Syn-DPyB* in the ground and excited states and the small energy differences between the states.

The kinetic analyses demonstrate that in *Anti-DPyB*, the (T_1T_1) formed through the excimer slowly dissociates into free triplets. On the other hand, it was also proposed that the intermolecular and

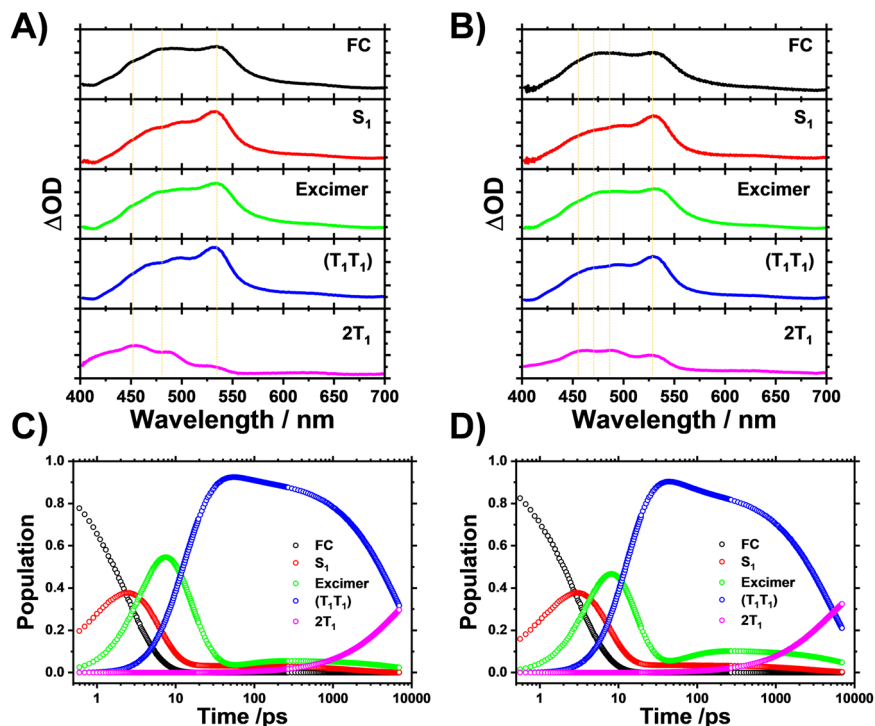


Fig. 6 Species-associated difference spectra and population changes of intermediates for *Syn*-DPyB obtained from the kinetic analysis for Kinetic Model (4) in *n*-hexane and acetonitrile. A, B Species-associated difference spectra in **A** *n*-hexane and **B** acetonitrile. **C, D** Population changes of intermediates in **C** *n*-hexane and **D** acetonitrile. The solid lines are the concentrations obtained from the kinetics analysis. The open circles represent the measure time delays.

intramolecular SF dynamics can rapidly occur with a direct process from the S_1 state to the free state due to strong coupling between the S_1 state and the free triplet state^{59–61}. For example, Dover et al. suggested that the SF channel is dominated by a direct mechanism from the S_1 state and the formation of the excimer state inhibits efficient SF dynamics⁶¹. Thus, we also explored the possibility that our data from *Anti*-DPyB and *Syn*-DPyB can be explained using the same direct mechanism by applying the kinetic analysis with the reaction schemes compatible with the direct SF mechanism (see Supplementary Fig. S27). Those reaction schemes involving a direct SF process did not satisfactorily reproduce the measured TA spectra for *Anti*-DPyB in *n*-hexane and acetonitrile or yielded an unphysical SADS curve (Supplementary Information and Supplementary Fig. S28). This result indicates that the coupling between the S_1 state and the free triplet state in CLDs such as *Anti*-DPyB and *Syn*-DPyB is weaker than in the molecules that showed such direct SF processes, although further systematic studies are needed to confirm this hypothesis.

Conclusions

To understand the ultrafast excited-state relaxation dynamics of intramolecular SF materials such as a CLD, we elucidated the ultrafast excited-state relaxation dynamics of covalently linked pyrene dimers *Anti*-DPyB and *Syn*-DPyB. In the excited state, *Anti*-DPyB, in which two Py moieties are oriented in a twisted configuration, forms the excimer through a conformational change with time constants of 231 and 24.3 ps in *n*-hexane and acetonitrile, respectively (Fig. 7). *Syn*-DPyB, with a pre-stacked configuration, rapidly forms the excimer without any conformational change with a time constant of ~ 3 ps. Our results also demonstrated that the excimer emissions observed from *Anti*-DPyB and *Syn*-DPyB are not prompt but delayed emissions. The time-resolved spectroscopic results showed that the resulting excimers rapidly relax to the (T_1T_1) state, suggesting that the (T_1T_1) 's of *Anti*-DPyB and

Syn-DPyB are formed through the excimer state. The (T_1T_1) of *Anti*-DPyB dissociates to free triplets as the end product, completing SF, whereas the dissociation reaction of (T_1T_1) in *Syn*-DPyB is significantly suppressed compared to *Anti*-DPyB. This means that *Anti*-DPyB forms unbound (T_1T_1) , resulting in efficient SF dynamics, whereas *Syn*-DPyB forms bound (T_1T_1) . The suppressed dissociation of (T_1T_1) into free triplets in *Syn*-DPyB is probably due to the triplet–triplet annihilation. This result differs from the prediction based on theoretical studies proposing that *meta*-linked dimers with a smaller E_b , compared with *ortho*- and *para*-linked dimers, exhibit efficient SF dynamics. This finding suggests that the efficiency of SF dynamics in CLDs cannot be predicted solely by the substitution position of the chromophore in a CLD. As *Anti*-DPyB and *Syn*-DPyB have relatively more distorted structures than previously studied CLDs (Fig. 1A), the orbital interaction likely has a much greater effect on their SF dynamics than the substitution position. Indeed, our data show that the relatively more efficient SF in *Anti*-DPyB compared to *Syn*-DPyB is caused by the relatively low electronic coupling between two chromophores owing to their twisted alignment. This result indicates that the SF dynamics in *ortho*-linked dimers, which generally show a significant π -orbital overlap between two chromophores, can be modulated by the control of the molecular configuration, consequently suggesting that the molecular geometry of a CLD plays a critical role in its SF dynamics, excimer formation, and ICT.

Methods

Synthetic procedures for *Anti*-DPyB and *Syn*-DPyB. See Supplementary Methods and Supplementary Fig. S1 in the Supplementary Information.

Characterization for *Anti*-DPyB and *Syn*-DPyB. See Supplementary Figs. S2–S5 for ^1H - and ^{13}C -NMR spectra and Supplementary Fig. S6 for GC–MS data.

Preparation of single crystal *Anti*-DPyB. See Supplementary Methods.

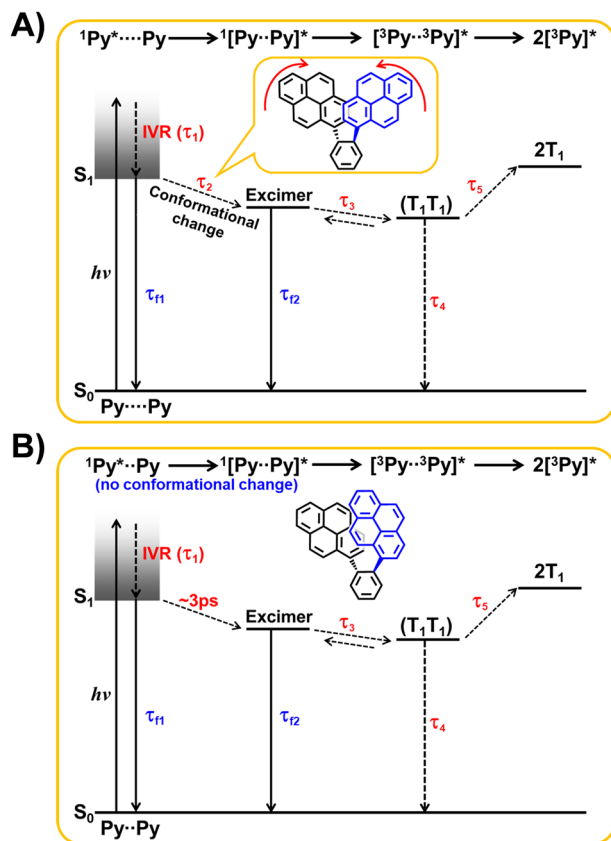


Fig. 7 Schematics for proposed relaxation dynamics of Anti-DPyB and Syn-DPyB. Excited-state relaxation dynamics of **A** Anti-DPyB and **B** Syn-DPyB. IVR stands for intramolecular vibrational relaxation.

X-ray crystal structure analysis. See Supplementary Methods, Supplementary Tables S1–S6, and Supplementary Fig. S7 for the thermal ellipsoid plot of Anti-DPyB.

Steady-state and time-resolved spectroscopic measurements. See Supplementary Methods, Supplementary Fig. S8 for fluorescence excitation spectra, Supplementary Fig. S9 for emission spectra of Py, Ph-Py, Anti-DPyB, and Syn-DPyB at 77 K, Supplementary Fig. S10 for femtosecond TA spectra of Anti-DPyB and Syn-DPyB, Supplementary Fig. S14 for nanosecond TA spectra of Anti-DPyB, Supplementary Fig. S16 for the concentration dependence of the emission spectra of Anti-DPyB and Syn-DPyB, Supplementary Fig. S17 for nanosecond TA spectra of 1-(2-bromophenyl)pyrene, Supplementary Fig. S18 for nanosecond TA spectra of Py, Ph-Py, Anti-DPyB, and Syn-DPyB, and Supplementary Fig. S19 for time profiles for transient absorption bands of Anti-DPyB and Syn-DPyB.

Cyclic voltammograms of Py, Anti-DPyB, and Syn-DPyB. See Supplementary Fig. S15.

Triplet quantum yield (Φ_T) of Anti-DPyB. See Supplementary Methods.

Time-resolved EPR spectroscopy. See Supplementary Methods and Supplementary Figs. S20 and S21.

Singular value decomposition (SVD) analysis. Details regarding SVD analysis are provided in the Supplementary Methods. The SVD analysis results (Supplementary Figs. S11 and S12) and the fits of rSVs (Supplementary Fig. S13) are provided in the Supplementary Methods.

Kinetic analysis. See Supplementary Methods. The results for the kinetic analysis of the TA spectra of Anti-DPyB and Syn-DPyB are given in Supplementary Figs. S22–S26.

Direct SF mechanisms from the S_1 state. See Supplementary Methods and Supplementary Figs. S27 and S28.

Cartesian coordinates from computational studies. See Supplementary Data 2.

Data availability

All data generated during this study are all provided in the Article and its Supplementary Information, but are available from the authors upon reasonable request. Cartesian coordinates from computational studies can be found in Supplementary Data 2. The X-ray crystallographic coordinate for Anti-DPyB reported in this Article has been deposited at the Cambridge Crystallographic Data Centre (CCDC), under deposition number CCDC-2089494. This data can be obtained free of charge from The Cambridge Crystallographic Data Centre via www.ccdc.cam.ac.uk/data_request/cif. The cif file for Anti-DPyB can be found in Supplementary Data 1.

Received: 18 October 2021; Accepted: 9 January 2023;

Published online: 17 January 2023

References

- Yu, Y. et al. Fast photoelectric conversion in the near-infrared enabled by plasmon-induced hot-electron transfer. *Adv. Mater.* **31**, 1903829 (2019).
- Gasparini, N. et al. Designing ternary blend bulk heterojunction solar cells with reduced carrier recombination and a fill factor of 77%. *Nat. Energy* **1**, 16118 (2016).
- Li, Y. R. et al. Implementing metal-to-ligand charge transfer in organic semiconductor for improved visible-near-infrared photocatalysis. *Adv. Mater.* **28**, 6959–6965 (2016).
- Ni, Z. Y. et al. Plasmonic silicon quantum dots enabled high-sensitivity ultrabroadband photodetection of graphene-based hybrid phototransistors. *ACS Nano* **11**, 9854–9862 (2017).
- Cheng, R. Q. et al. High-performance, multifunctional devices based on asymmetric van der Waals heterostructures. *Nat. Electron.* **1**, 356–361 (2018).
- Ren, P. et al. Global performance evaluation of solar cells using two models: from charge-transfer and recombination mechanisms to photoelectric properties. *J. Mater. Chem. C* **7**, 1934–1947 (2019).
- Rao, A. & Friend, R. H. Harnessing singlet exciton fission to break the Shockley–Queisser limit. *Nat. Rev. Mater.* **2**, 17063 (2017).
- Grabowski, Z. R., Rotkiewicz, K. & Rettig, W. Structural changes accompanying intramolecular electron transfer: focus on twisted intramolecular charge-transfer states and structures. *Chem. Rev.* **103**, 3899–4031 (2003).
- Kim, S. et al. Charge transfer induced by electronic state mixing in a symmetric X–Y–X-type multi-chromophore system. *Phys. Chem. Chem. Phys.* **22**, 28440–28447 (2020).
- Adams, D. M. et al. Charge transfer on the nanoscale: current status. *J. Phys. Chem. B* **107**, 6668–6697 (2003).
- Břédas, J.-L., Beljonne, D., Coropceanu, V. & Cornil, J. Charge-transfer and energy-transfer processes in π -conjugated oligomers and polymers: a molecular picture. *Chem. Rev.* **104**, 4971–5004 (2004).
- Chen, M. et al. Singlet fission in covalent terrylenediimide dimers: probing the nature of the multiexciton state using femtosecond mid-infrared spectroscopy. *J. Am. Chem. Soc.* **140**, 9184–9192 (2018).
- Dean, J. C. et al. Photophysical characterization and time-resolved spectroscopy of an anthradithiophene dimer: exploring the role of conformation in singlet fission. *Phys. Chem. Chem. Phys.* **19**, 23162–23175 (2017).
- Yamakado, T. et al. Conformational planarization versus singlet fission: distinct excited-state dynamics of cyclooctatetraene-fused acene dimers. *Angew. Chem. Int. Ed.* **57**, 5438–5443 (2018).
- Nakamura, S. et al. Synergetic role of conformational flexibility and electronic coupling for quantitative intramolecular singlet fission. *J. Phys. Chem. C* **125**, 18287–18296 (2021).
- Paul, S., Govind, C. & Karunakaran, V. Planarity and length of the bridge control rate and efficiency of intramolecular singlet fission in pentacene dimers. *J. Phys. Chem. B* **125**, 231–239 (2021).
- Monahan, N. & Zhu, X. Y. Charge transfer-mediated singlet fission. *Annu. Rev. Phys. Chem.* **66**, 601–618 (2015).
- Holtén, D., Bocian, D. F. & Lindsey, J. S. Probing electronic communication in covalently linked multiporphyrin arrays. a guide to the rational design of molecular photonic devices. *Acc. Chem. Res.* **35**, 57–69 (2002).
- Popp, W., Brey, D., Binder, R. & Burghardt, I. Quantum dynamics of exciton transport and dissociation in multichromophoric systems. *Annu. Rev. Phys. Chem.* **72**, 591–616 (2021).
- Oh, I. et al. Enhancement of energy transfer efficiency with structural control of multichromophore light-harvesting assembly. *Adv. Sci.* **7**, 2001623 (2020).
- Young, R. M. & Wasielewski, M. R. Mixed electronic states in molecular dimers: connecting singlet fission, excimer formation, and symmetry-breaking charge transfer. *Acc. Chem. Res.* **53**, 1957–1968 (2020).

22. Kim, S.-T., Hartman, R. F. & Rose, S. D. Solvent dependence of pyrimidine dimer splitting in a covalently linked dimer-indole system. *Photochem. Photobiol.* **52**, 789–794 (1990).
23. Kumarasamy, E. et al. Tuning singlet fission in π -bridge- π chromophores. *J. Am. Chem. Soc.* **139**, 12488–12494 (2017).
24. Hong, Y. et al. Efficient multiexciton state generation in charge-transfer-coupled perylene bisimide dimers via structural control. *J. Am. Chem. Soc.* **142**, 7845–7857 (2020).
25. Margulies, E. A. et al. Direct observation of a charge-transfer state preceding high-yield singlet fission in terrylenediimide thin films. *J. Am. Chem. Soc.* **139**, 663–671 (2017).
26. Alvertis, A. M. et al. Switching between coherent and incoherent singlet fission via solvent-induced symmetry breaking. *J. Am. Chem. Soc.* **141**, 17558–17570 (2019).
27. Pun, A. B. et al. Ultra-fast intramolecular singlet fission to persistent multiexcitons by molecular design. *Nat. Chem.* **11**, 821–828 (2019).
28. Smith, M. B. & Michl, J. Recent advances in singlet fission. *Annu. Rev. Phys. Chem.* **64**, 361–386 (2013).
29. Zirzmeier, J. et al. Singlet fission in pentacene dimers. *Proc. Natl Acad. Sci. USA* **112**, 5325–5330 (2015).
30. Margulies, E. A. et al. Enabling singlet fission by controlling intramolecular charge transfer in π -stacked covalent terrylenediimide dimers. *Nat. Chem.* **8**, 1120–1125 (2016).
31. Busby, E. et al. A design strategy for intramolecular singlet fission mediated by charge-transfer states in donor–acceptor organic materials. *Nat. Mater.* **14**, 426–433 (2015).
32. Smith, M. B. & Michl, J. Singlet fission. *Chem. Rev.* **110**, 6891–6936 (2010).
33. Johnson, J. C., Nozik, A. J. & Michl, J. The role of chromophore coupling in singlet fission. *Acc. Chem. Res.* **46**, 1290–1299 (2013).
34. Walker, B. J., Musser, A. J., Beljonne, D. & Friend, R. H. Singlet exciton fission in solution. *Nat. Chem.* **5**, 1019–1024 (2013).
35. Stern, H. L. et al. Vibronically coherent ultrafast triplet-pair formation and subsequent thermally activated dissociation control efficient endothermic singlet fission. *Nat. Chem.* **9**, 1205–1212 (2017).
36. Schultz, J. D. et al. Influence of vibronic coupling on ultrafast singlet fission in a linear terrylenediimide dimer. *J. Am. Chem. Soc.* **143**, 2049–2058 (2021).
37. Lukman, S. et al. Tuning the role of charge-transfer states in intramolecular singlet exciton fission through side-group engineering. *Nat. Commun.* **7**, 13622 (2016).
38. Ni, W. et al. Singlet fission from upper excited electronic states of cofacial perylene dimer. *J. Phys. Chem. Lett.* **10**, 2428–2433 (2019).
39. Korovina, N. V. et al. Linker-dependent singlet fission in tetracene dimers. *J. Am. Chem. Soc.* **140**, 10179–10190 (2018).
40. Shizu, K., Adachi, C. & Kaji, H. Effect of vibronic coupling on correlated triplet pair formation in the singlet fission process of linked tetracene dimers. *J. Phys. Chem. A* **124**, 3641–3651 (2020).
41. Chesler, R., Khan, S. & Mazumdar, S. Wave function based analysis of dynamics versus yield of free triplets in intramolecular singlet fission. *J. Phys. Chem. A* **124**, 10091–10099 (2020).
42. Abraham, V. & Mayhall, N. J. Simple rule to predict boundedness of multiexciton states in covalently linked singlet-fission dimers. *J. Phys. Chem. Lett.* **8**, 5472–5478 (2017).
43. Zirzmeier, J. et al. Solution-based intramolecular singlet fission in cross-conjugated pentacene dimers. *Nanoscale* **8**, 10113–10123 (2016).
44. Jo, S. et al. UV/Vis absorption spectrum calculations of benzo-1,2-dipyrene isomer using long-range corrected density functional theory. *Chem. Phys. Lett.* **761**, 138023 (2020).
45. Crawford, A. G. et al. Experimental and theoretical studies of the photophysical properties of 2- and 2,7-functionalized pyrene derivatives. *J. Am. Chem. Soc.* **133**, 13349–13362 (2011).
46. Birks, J. B. & Christophorou, L. G. Excimer fluorescence spectra of pyrene derivatives. *Spectrochim. Acta* **19**, 401–410 (1963).
47. Van Dyke, D. A., Pryor, B. A., Smith, P. G. & Topp, M. R. Nanosecond time-resolved fluorescence spectroscopy in the physical chemistry laboratory: formation of the pyrene excimer in solution. *J. Chem. Educ.* **75**, 615 (1998).
48. D'Aleo, A., Cecchetto, E., De Cola, L. & Williams, R. M. Metal ion enhanced charge transfer in a terpyridine-bis-pyrene system. *Sensors* **9**, 3604–3626 (2009).
49. Rajagopal, S. K., Mallia, A. R. & Hariharan, M. Enhanced intersystem crossing in carbonylpyrenes. *Phys. Chem. Chem. Phys.* **19**, 28225–28231 (2017).
50. Nakamura, T., Kira, A. & Imamura, M. Enhancement of the intersystem crossing of pyrene by metal ions in sodium dodecyl sulfate micelle solutions. *J. Phys. Chem.* **86**, 3359–3363 (1982).
51. Langelaar, J., Rettschnick, R. P. H. & Hooijtink, G. J. Studies on triplet radiative lifetimes, phosphorescence, and delayed fluorescence yields of aromatic hydrocarbons in liquid solutions. *J. Chem. Phys.* **54**, 1–7 (1971).
52. Mauck, C. M. et al. Singlet fission via an excimer-like intermediate in 3,6-bis(thiophen-2-yl)diketopyrrolopyrrole derivatives. *J. Am. Chem. Soc.* **138**, 11749–11761 (2016).
53. Tamura, H. Triplet exciton transfers and triplet-triplet annihilation in anthracene derivatives via direct versus superexchange pathways governed by molecular packing. *J. Phys. Chem. A* **124**, 7943–7949 (2020).
54. Lin, H.-H., Kue, K. Y., Claudio, G. C. & Hsu, C.-P. First principle prediction of intramolecular singlet fission and triplet triplet annihilation rates. *J. Chem. Theory Comput.* **15**, 2246–2253 (2019).
55. Müller, A. M., Avlasevich, Y. S., Schoeller, W. W., Müllen, K. & Bardeen, C. J. Exciton fission and fusion in bis(tetracene) molecules with different covalent linker structures. *J. Am. Chem. Soc.* **129**, 14240–14250 (2007).
56. Kolomeisky, A. B., Feng, X. & Krylov, A. I. A simple kinetic model for singlet fission: a role of electronic and entropic contributions to macroscopic rates. *J. Phys. Chem. C* **118**, 5188–5195 (2014).
57. Ito, S., Nagami, T. & Nakano, M. Design principles of electronic couplings for intramolecular singlet fission in covalently-linked systems. *J. Phys. Chem. A* **120**, 6236–6241 (2016).
58. Ito, S., Nagami, T. & Nakano, M. Rational design of doubly-bridged chromophores for singlet fission and triplet-triplet annihilation. *RSC Adv.* **7**, 34830–34845 (2017).
59. Fuemmeler, E. G. et al. A direct mechanism of ultrafast intramolecular singlet fission in pentacene dimers. *ACS Cent. Sci.* **2**, 316–324 (2016).
60. Fumanal, M. & Corminboeuf, C. Direct, mediated, and delayed intramolecular singlet fission mechanism in donor–acceptor copolymers. *J. Phys. Chem. Lett.* **11**, 9788–9794 (2020).
61. Dover, C. B. et al. Endothermic singlet fission is hindered by excimer formation. *Nat. Chem.* **10**, 305–310 (2018).

Acknowledgements

This work was supported by the Institute for Basic Science (IBS-R033). This work was supported by the National Research Foundation of Korea (NRF), funded by the Ministry of Education (NRF-2020R1C1C1009007 and NRF-2017M3D1A1039380).

Author contributions

J.C., K.-R.W., and H.I. designed research; J.C., S.K., M.A., J.K., D.W.C., D.K., S.E., D.I., Y.K., S.H.K., K.-R.W., and H.I. performed research; J.C., S.K., M.A., J.K., D.W.C., D.K., S.E., D.I., Y.K., S.H.K., K.-R.W., and H.I. contributed interpretation of results and J.C., K.-R.W., and H.I. wrote the paper.

Competing interests

The authors declare no competing interests.

Additional information

Supplementary information The online version contains supplementary material available at <https://doi.org/10.1038/s42004-023-00816-6>.

Correspondence and requests for materials should be addressed to Kyung-Ryang Wee or Hyotcherl Ihee.

Peer review information *Communications Chemistry* thanks the anonymous reviewers for their contribution to the peer review of this work. Peer reviewer reports are available.

Reprints and permission information is available at <http://www.nature.com/reprints>

Publisher's note Springer Nature remains neutral with regard to jurisdictional claims in published maps and institutional affiliations.



Open Access This article is licensed under a Creative Commons Attribution 4.0 International License, which permits use, sharing, adaptation, distribution and reproduction in any medium or format, as long as you give appropriate credit to the original author(s) and the source, provide a link to the Creative Commons license, and indicate if changes were made. The images or other third party material in this article are included in the article's Creative Commons license, unless indicated otherwise in a credit line to the material. If material is not included in the article's Creative Commons license and your intended use is not permitted by statutory regulation or exceeds the permitted use, you will need to obtain permission directly from the copyright holder. To view a copy of this license, visit <http://creativecommons.org/licenses/by/4.0/>.

© The Author(s) 2023